SUPPLEMENTARY INFORMATION FOR

Towards the development of a Z-scheme FeOx/g-C_3N_4 thin film and perspectives for ciprofloxacin visible light-driven photocatalytic degradation

Murilo Fendrich [1], Om Prakash Bajpai [1], Raju Edla [1], Alessandra Molinari [2], Paola Ragonese [3], Chiara Maurizio [3], Michele Orlandi [1] and Antonio Miotello [1,*]

[1] Physics Department, University of Trento, via Sommarive 14, 38123 Povo, Trento, Italy
[2] Department of Chemical, Pharmaceutical and Agricultural Sciences, University of Ferrara, Via L. Borsari 46, Ferrara 44121, Italy
[3] Physics and Astronomy Department and CNISM, University of Padova, via Marzolo 8, I-35131 Padova, Italy
* Correspondence: author: antonio.miotello@unitn.it

S1. Different aspects regarding ex situ and in situ materials synthesis methods

As g-C_3N_4 powder synthesis is well studied, in case of the ex situ method, we selected an optimised 4 hour annealing time based on the extensive literature available on the synthesis of g-C_3N_4 from melamine [1–4]. However, in the in situ case, given the known low yields of melamine conversion to g-C_3N_4 and small masses involved on FeOx, we did not observe g-C_3N_4 film formation in the 4h duration of annealing. Therefore, in the in situ method, g-C_3N_4 film formation was optimised for 1h and 2h duration on the bare glass slide, i.e., without FeOx. During the optimisation in the 1h case, we obtained a more uniform film. For the 2h case, very little g-C_3N_4 with an uneven film formation was observed. This is possibly due to the higher evaporation of melamine from the glass slide throughout the longer duration of annealing, especially in the case of the in situ method where a small amount of melamine in suspension (approximately 20 drops of 100 mg/mL concentrated suspension with ethanol) was dispersed in a large area (glass slide 7.5 × 2.5 cm) in comparison to the ex situ case (where a bulk amount of melamine powder, i.e., 10g, was directly annealed in a porcelain crucible).

S2. Light source for Photocatalysis Experiments

The following spectra were acquired using a portable mini spectrometer, model Hamamatsu C10082CA series, sensor S10420-1106N-01.

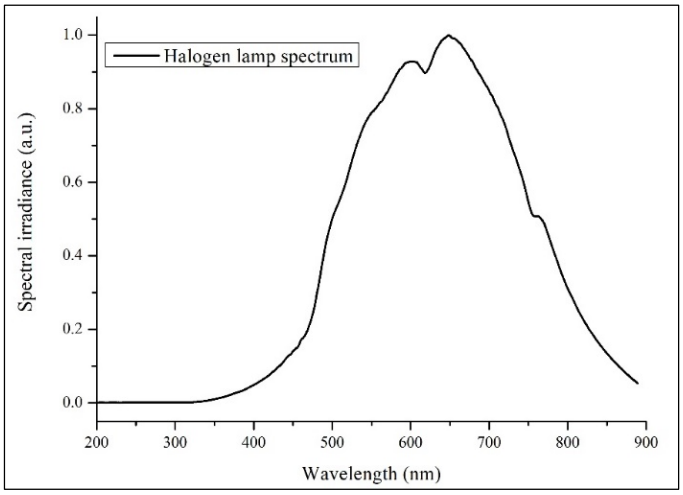

Figure S1. Measured and normalized spectrum of visible light lamps (75W each) employed in this work (Osram HALOPAR 30, 75W, 30° aperture angle, luminous flux of 350 lumens).

S3. Characterization of Materials—g-C_3N_4 bulk

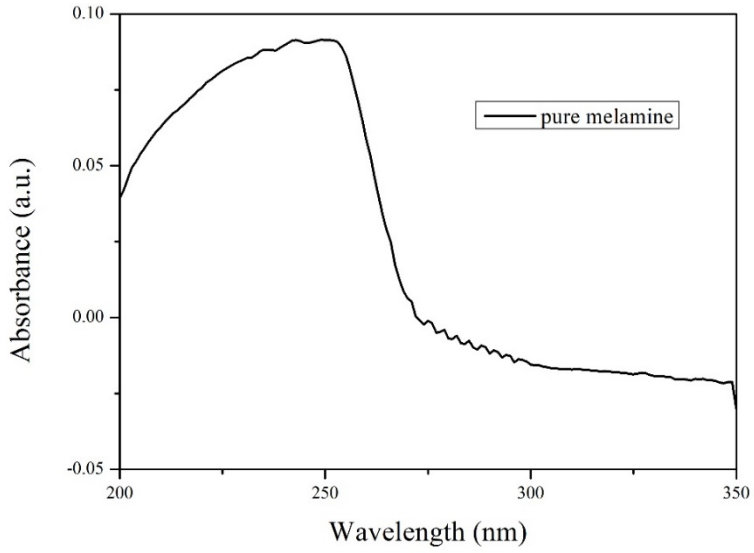

Figure S2. Absorption spectrum of melamine used as precursor to g-C_3N_4 synthesis.

The optical absorption spectrum of melamine as a function of wavelength is reported in Fig. S2, while the morphology and composition of the synthesized powders were investigated using the SEM technique, and results are reported in Fig. S3. Nanoparticles of sizes of hundreds of nanometres with compact structures are visible, possibly generated by the coalescence and rearrangement of the nanostructures. The corresponding EDXS spectra show the presence of only C and N.

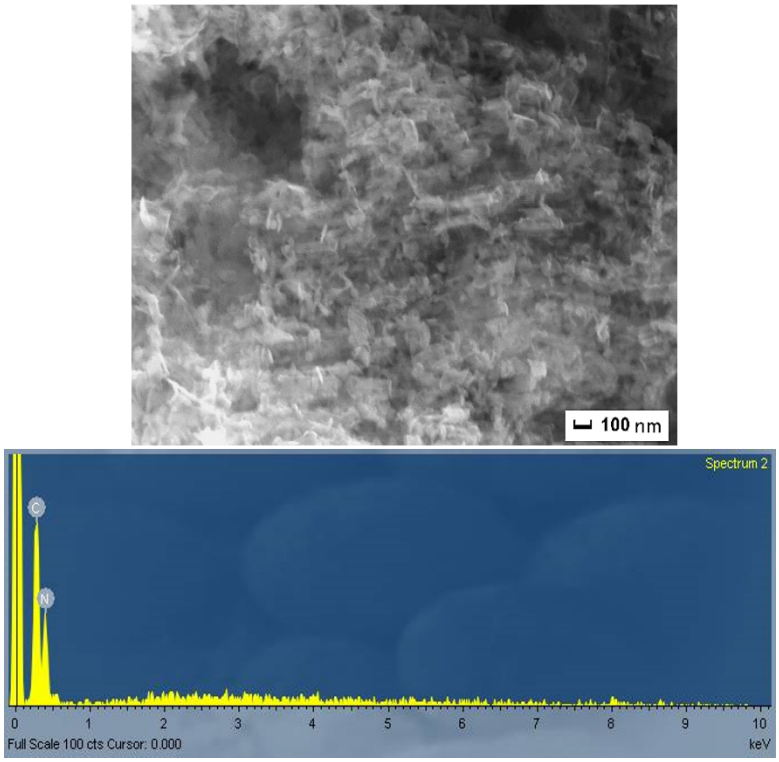

Figure S3. SEM image of g-C_3N_4 powder synthesized at 550 °C 4h and its corresponding EDXS spectra.

Fig. S4 presents FTIR characterization. In the conversion of melamine to g-C_3N_4 [5], the peaks at 3472, 3417, and 3325 cm^{-1}, attributed to the stretching and deformation modes of $–NH_2$ groups, gradually decreased when the temperature increases gave rise to peaks at 3250, 3150, and 3080 cm^{-1}, indicating deamination. Meanwhile, the peaks at 875 and 804 cm^{-1}, which correspond to the stretching modes of the triazine ring, remain. Signals also appear in the 1200–1700 cm^{-1} region, which are related to the typical stretching modes of C=N and C–N hetero-cycles.

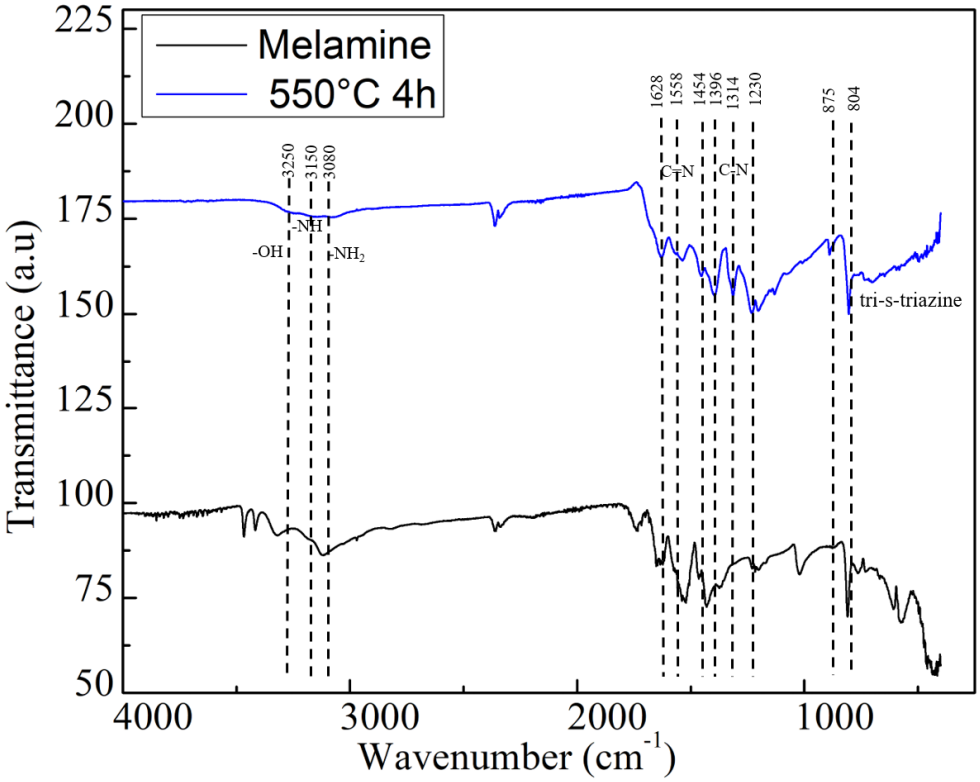

Figure S4. FTIR spectra of the melamine and g-C_3N_4 synthesized at 550 °C for 4h.

Micro-Raman analysis was used to investigate the conversion from melamine precursor to g-C_3N_4 at 550 °C for 4h. The results of the analysis are presented in Fig. S5. The Raman spectrum of melamine contains characteristic peaks at 155, 378, 581, 674, and 982 cm^{-1}, whereas g-C_3N_4 is identified by the peaks at 211, 359, 471, 588, 706, 768, 984, 1117, 1151, 1232, and 1312 cm^{-1}, respectively. Moreover, there are two less intense peaks at approximately 1360 cm^{-1} (D band) and 1580 cm^{-1} (G band) indicating the disordered sp^2 and graphite-like sp^2 microdomains, which confirm the formation of C–N [6,7]. Peaks assignments are found in Table S1.

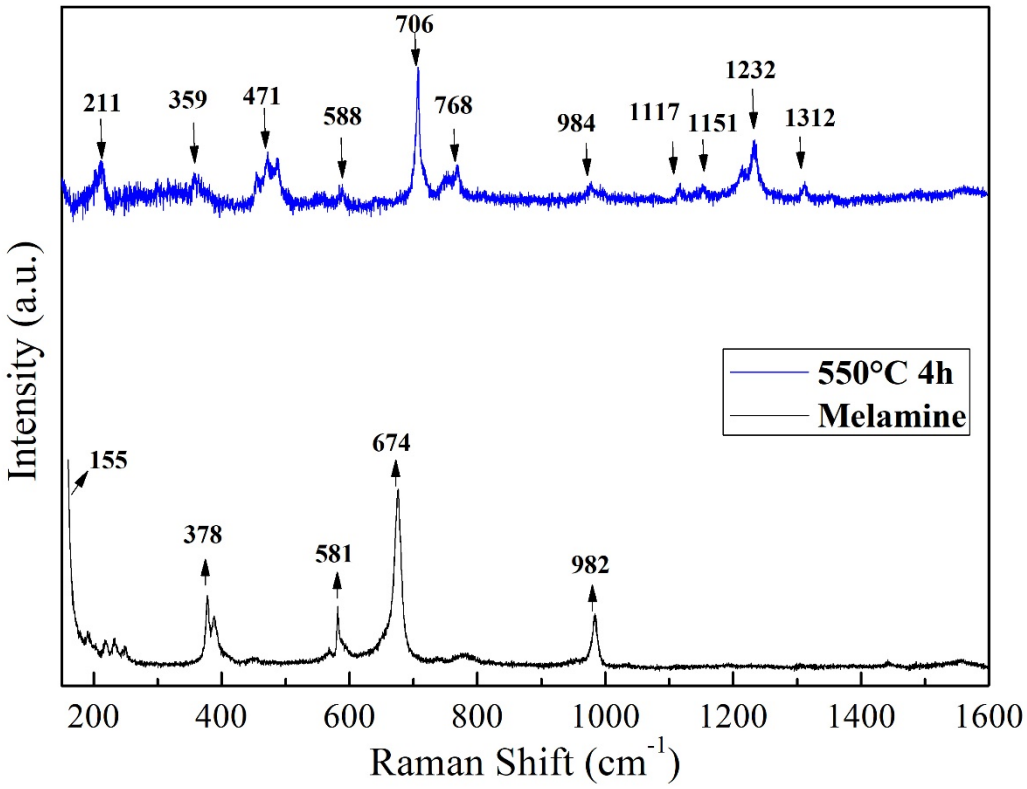

Figure S5. Raman spectra of melamine and g-C_3N_4 synthesized at 550 °C 4h.

X-rays analysis was performed to study the crystallinity of the obtained g-C_3N_4 powder (Fig. S6). The XRD pattern obtained confirms the formation of the graphitic-like phase of C_3N_4 lattice system. Indeed, the diffraction peak at 27.5° corresponds to typical (002) interlayer stacking of aromatic units in the heptazine chains and interplanar separation (JCPDS No. 87-1526).

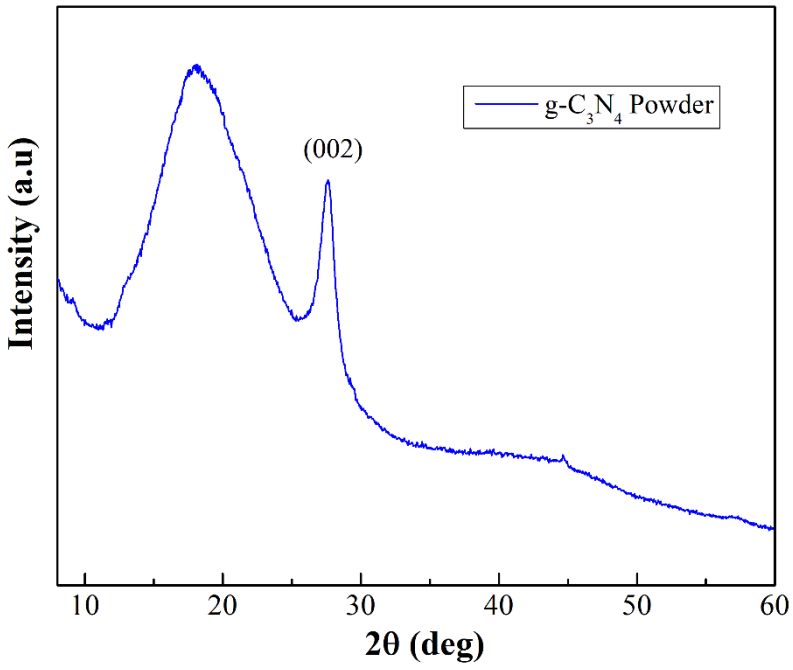

Figure S6. GIXRD pattern of the synthesized g-C_3N_4 powder at 550 °C.

The absorption spectra and Tauc plot of the synthesized g-C_3N_4 powder is presented in Fig. S7. An increase in UV absorbance is observed in the range 400–500nm, with a maximum at 400 nm and towards the UV region. Tauc plots show the direct bandgap, 2.92 eV, of the synthesized g-C_3N_4.

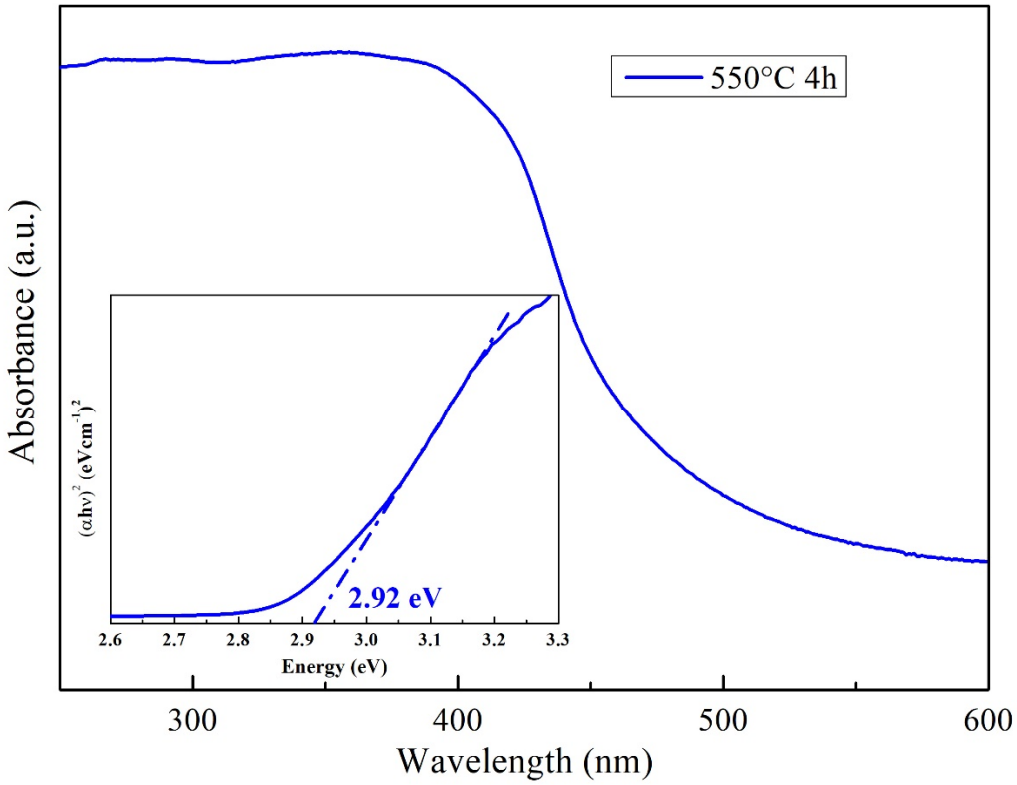

Figure S7. UV–Vis absorption spectra and Tauc plot of the g-C_3N_4 synthesized at 550 °C for 4h.

S4. Characterization of Materials—FeOx and Composites

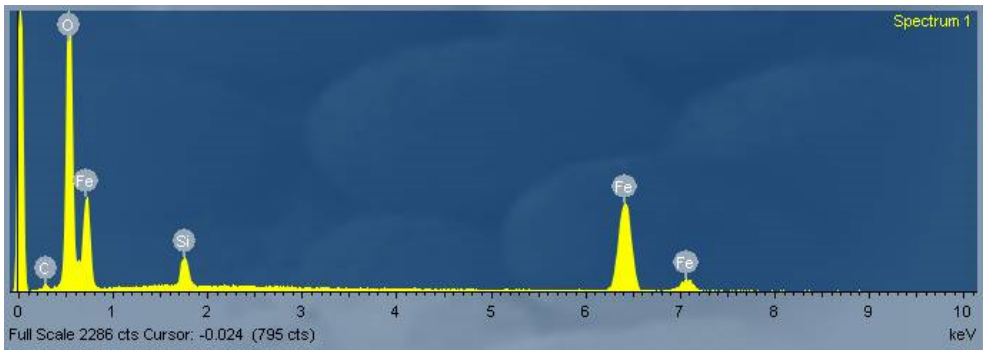

Figure S8. EDXS spectrum of the surface of the FeOx urchin-like structures used as a support in the composite with g-C_3N_4.

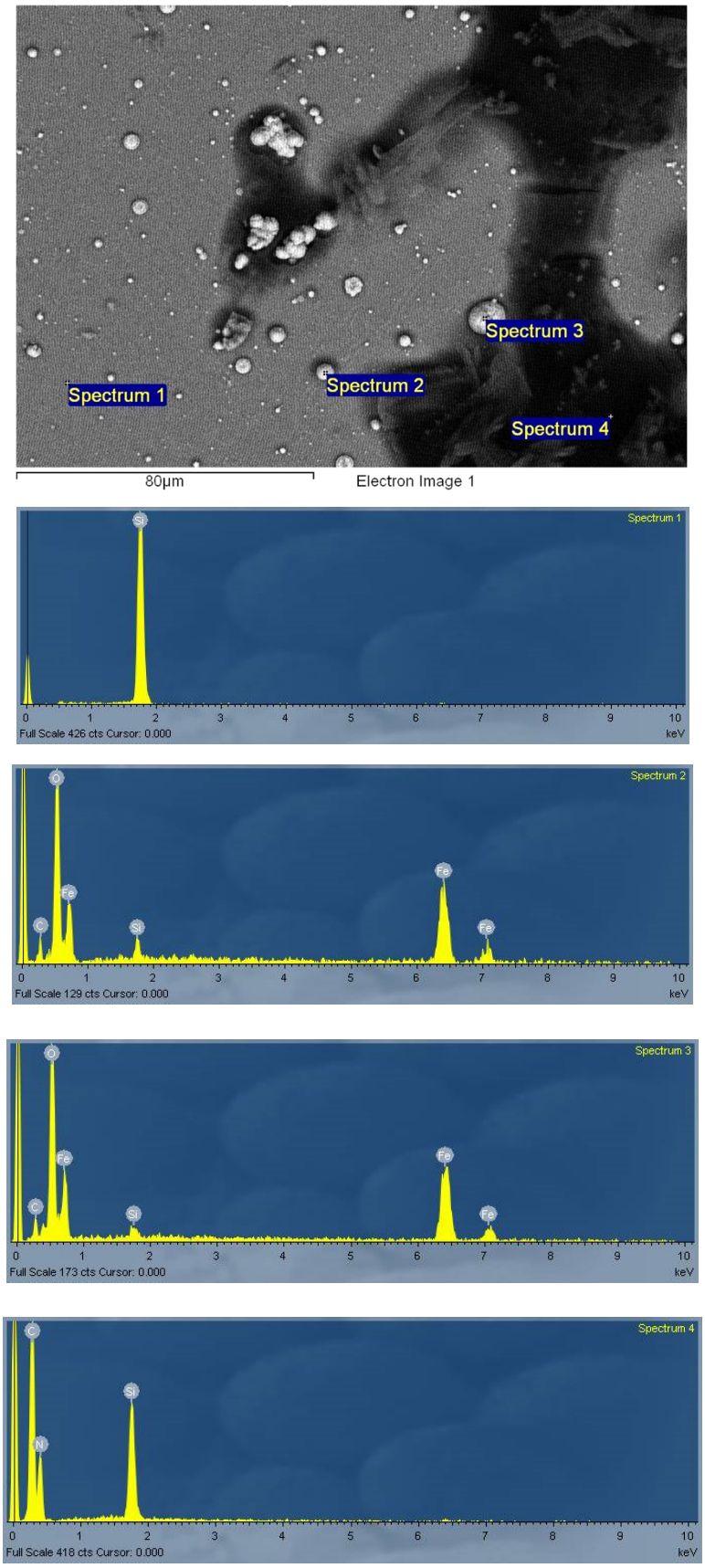

Figure S9. EDXS spectra from four different regions of the (FeOx/g-C_3N_4)*in* composite thin films.

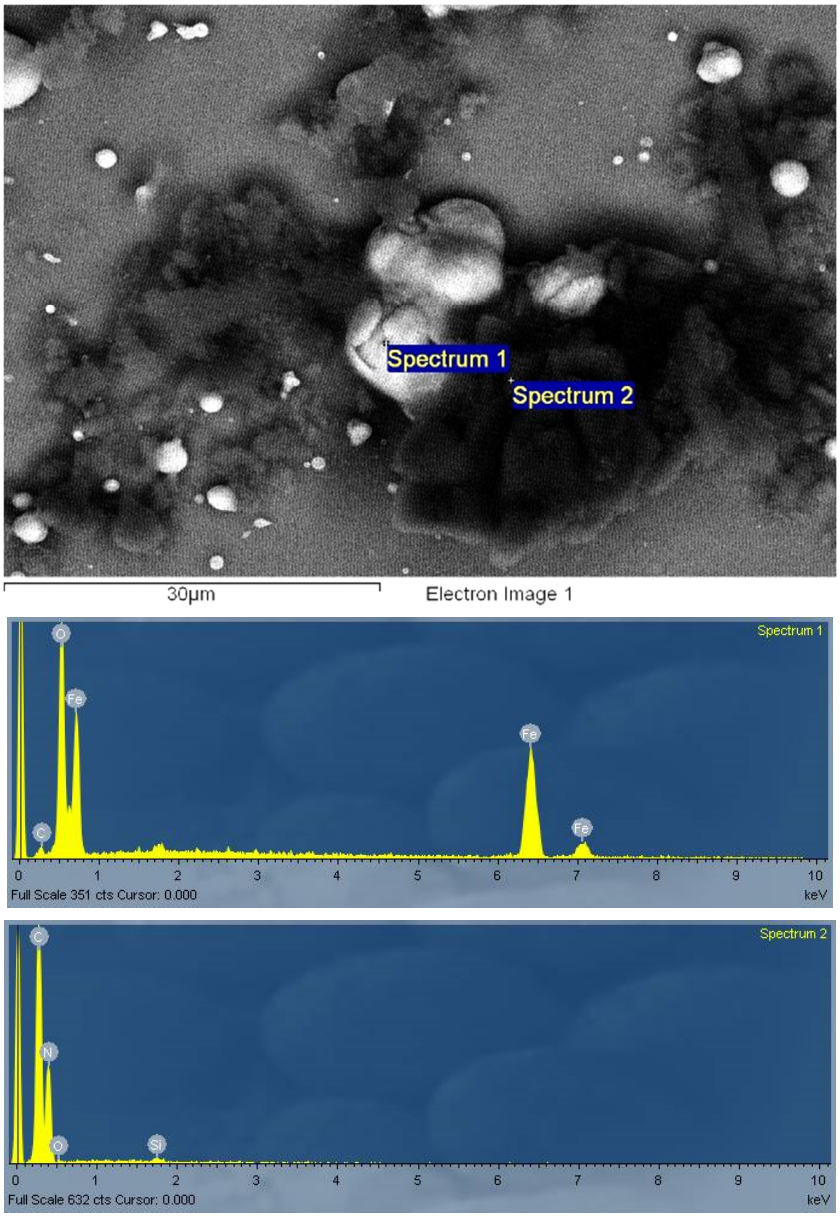

Figure S10. EDXS spectra from two different regions of the (FeOx/g-C_3N_4)*ex* composite thin films.

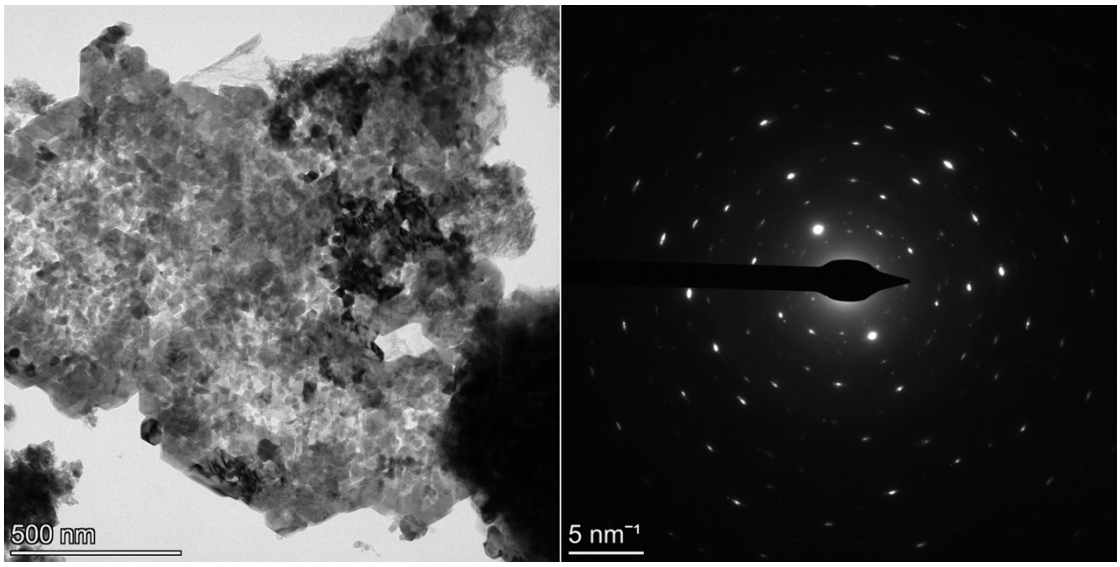

Figure S11. (FeOx/g-C_3N_4)*in* TEM image and corresponding larger area SAED pattern.

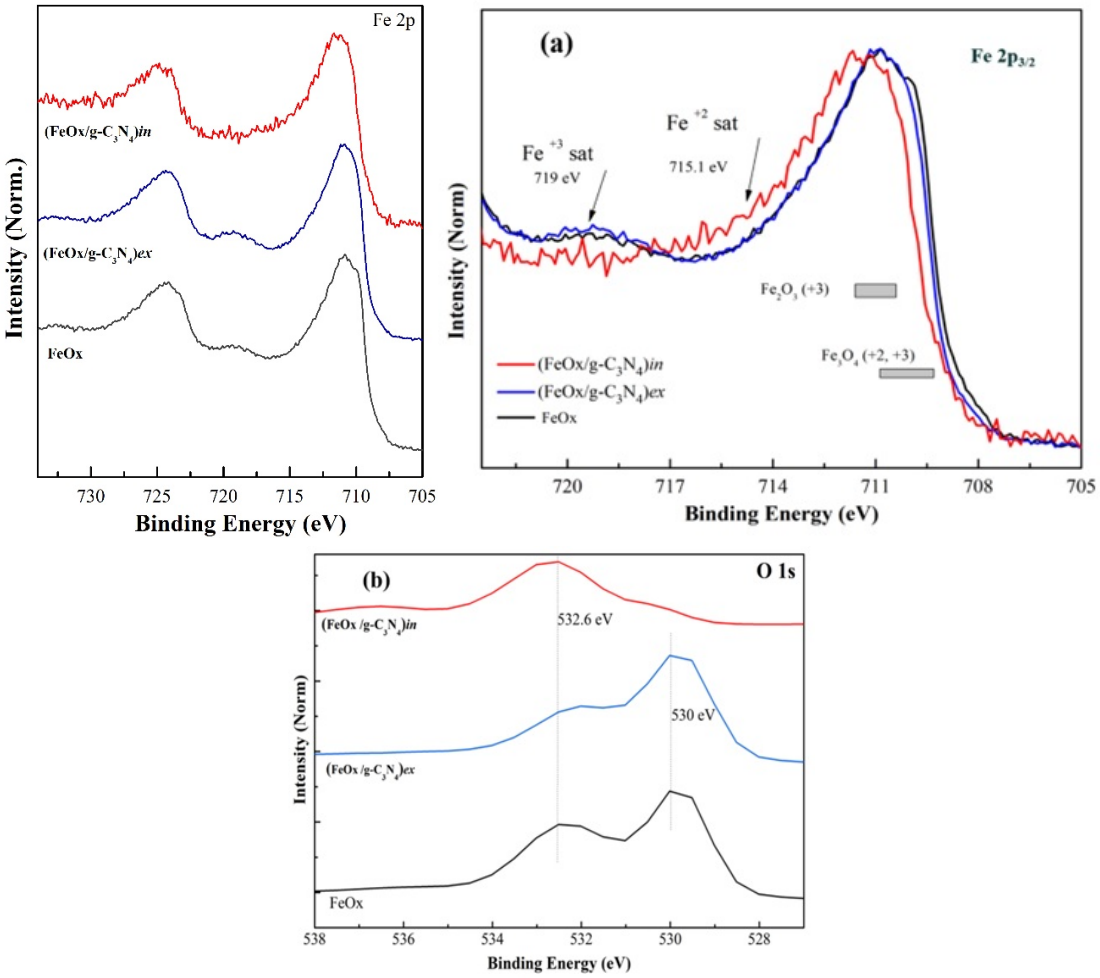

Figure S12. XPS spectra of (a) Fe 2p (top left) and specifically Fe $2p_{3/2}$ (top right) and (b) O1s core levels without the curve fitting of the iron urchin and its composites with g-C_3N_4.

S5. Supporting Information Regarding Photocatalytic Tests

The g-C_3N_4 dispersed powder (4h) (0.5g/L) and g-C_3N_4 (4h) coating material with a mass of 5mg for use as films were first studied. In a typical experiment, each photocatalyst was suspended or immersed in an aqueous solution (50 mL) containing CIP (C_0=10 ppm). Results are reported in Fig. S13. It is observed that after the period in the dark, nearly 40% of the CIP was adsorbed on the surface of the g-C_3N_4 powder. However, subsequent visible irradiation led to negligible decrease (less than 5%) in starting CIP. Concerning the coating, it exhibited low adsorption of CIP (around 4%) and an overall removal of 8%.

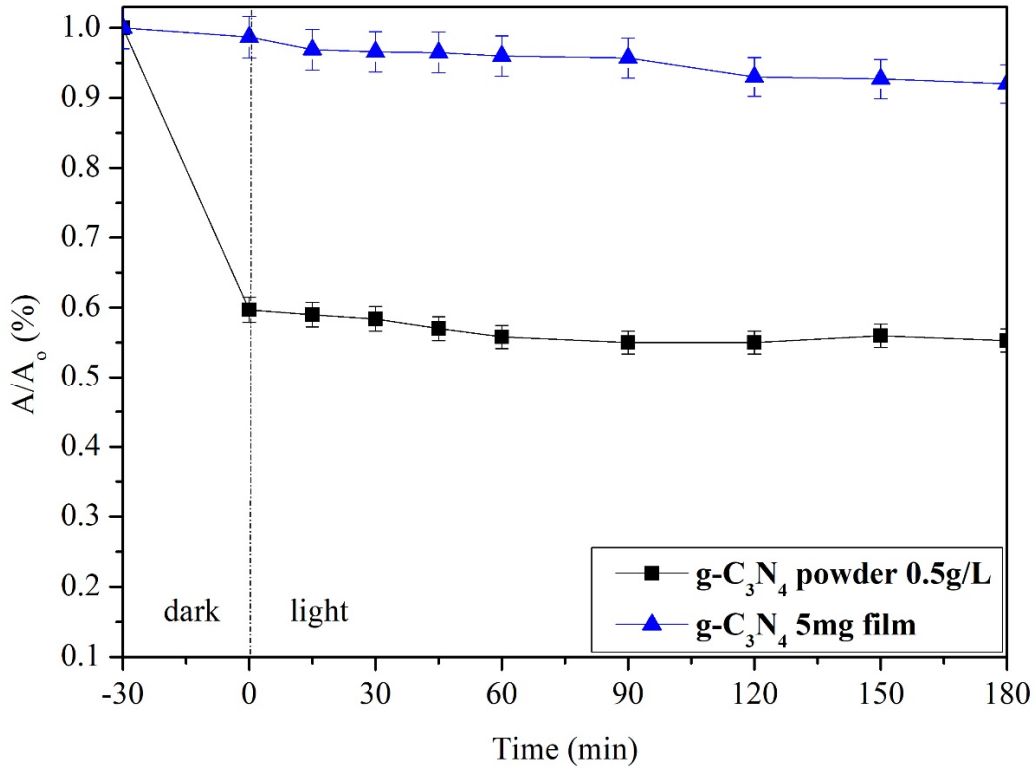

Figure S13. Removal yields of the CIP disappearance upon the irradiation of g-C_3N_4 4h in powder (black) and in the film (blue) in aqueous solutions containing CIP (C_0 = 10 ppm).

The (FeOx/g-C_3N_4)*ex* thin films led to poor (only 5%) CIP disappearance after 180 min of irradiation.

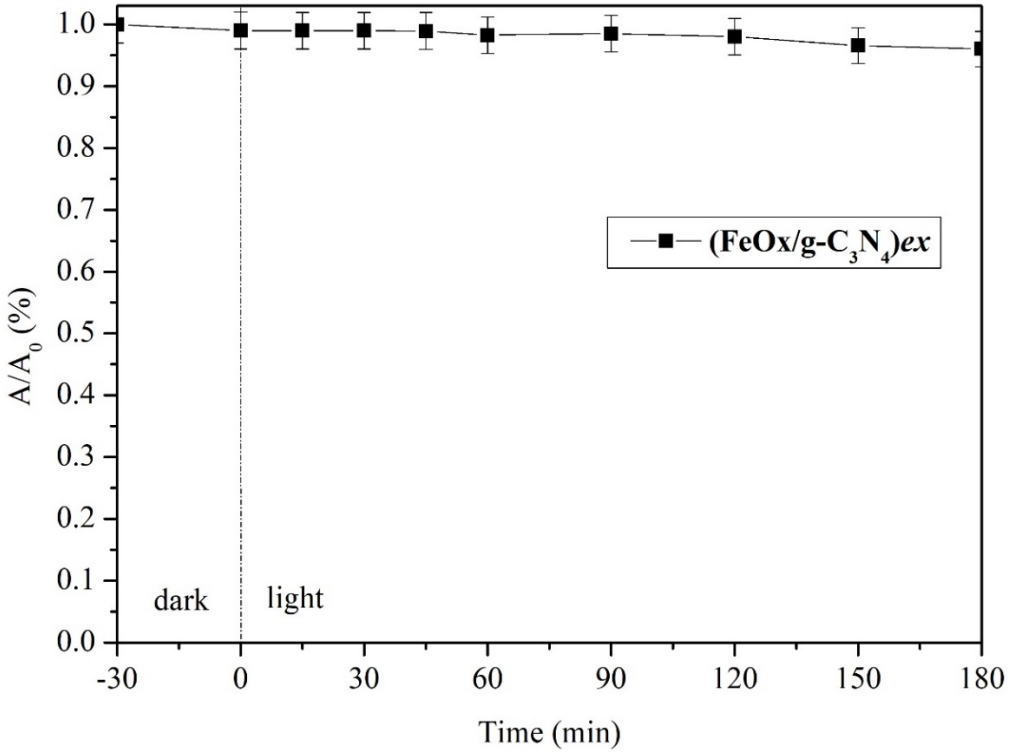

Figure S14. Removal yields of the CIP disappearance upon the irradiation of (FeOx/g-C_3N_4)*ex* thin films immersed in aqueous solutions containing CIP (C_0 = 10 ppm).

.

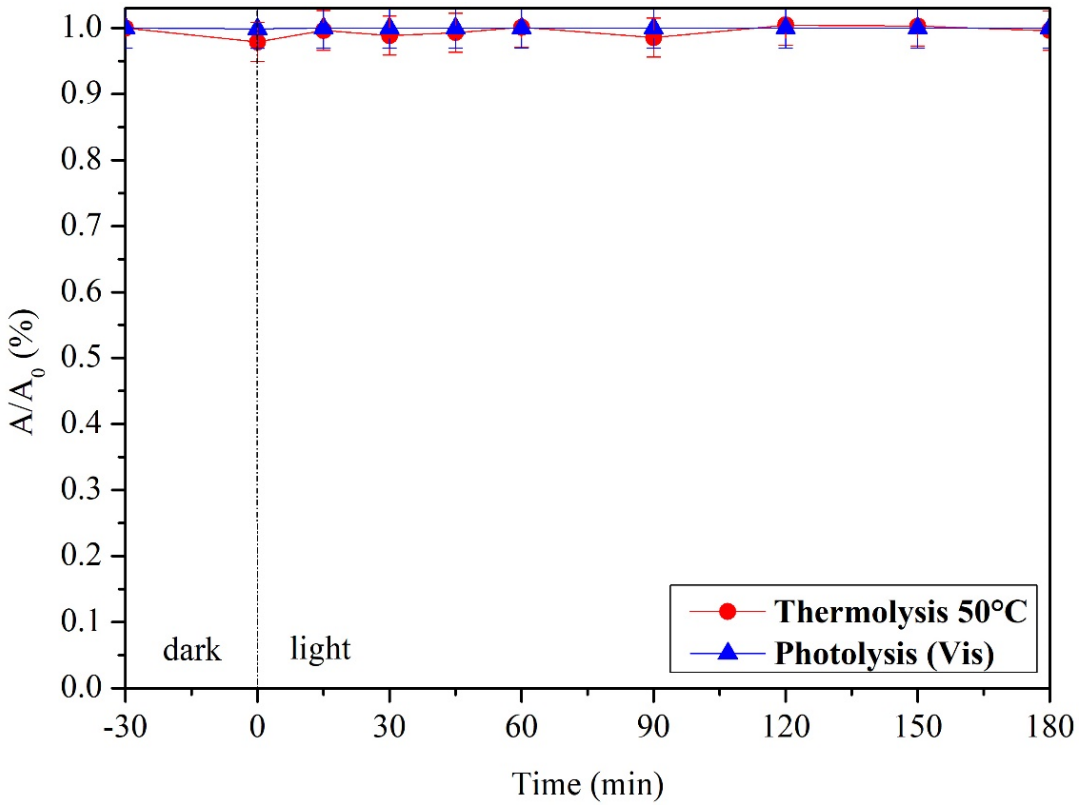

Figure S15. Control experiments: aerated aqueous solution of CIP (10 ppm) maintained at 50°C in the dark (red) or visible irradiated (blue) in the absence of any photocatalyst.

S6. Raman Peak Assignments

Table S1. The modes of every peak identified in the Raman measurements. The peak identifications are based on the literature [8–11].

Melamine	**Description of Vibration**	**Mode**
155		Unassigned
378	Quadrant out-of-plane bending	E’
581	Ring bending	A1
674	Quadrant in-plane bend, ring	E’
982	N radial, in-phase	A1’
Bulk g-C_3N_4 and (FeOx/g-C_3N_4)*ex*	**Description of Vibration**	**Mode**
211		Unassigned
359		Unassigned
471	Ring stretching	E’
588	Ring bending	A1
706	Heptazine ring breathing modes	A1’
768		A1’
984	N radial, in-phase	A1’
1117	C radial, in-phase	A1’
1151	Semi-circle stretching, NH_2 rocking	E’

1232	Typical stretching vibration modes of C=N and C–N heterocycles.	E’
1312	Semi-circle stretching	E’
	FeOx	**Mode**
	226	A1g
	245	Eg
	292	Eg
	410	Eg
	500	A1g
	613	Eg
	822	B_2O_3 on surface
	1313	2LO phonon–phonon
(FeOx/g-C_3N_4)*in*	**Description of Vibration**	**Mode**
170		Unassigned
298	Iron	Eg
521	Iron and C_3N_4	A1g / A1
749	Heptazine ring breathing modes	A1’
810	Boron and C_3N_4	A1’
999	N radial, in-phase	A1’
1156	Semi-circle stretching, NH_2 rocking	E’
1266	Typical stretching vibration modes of C=N and C–N heterocycles.	E’
1346	Semi-circle stretching	E’
1386	Iron	2LO

S7. UV–visible spectra from the photocatalysis experiments.

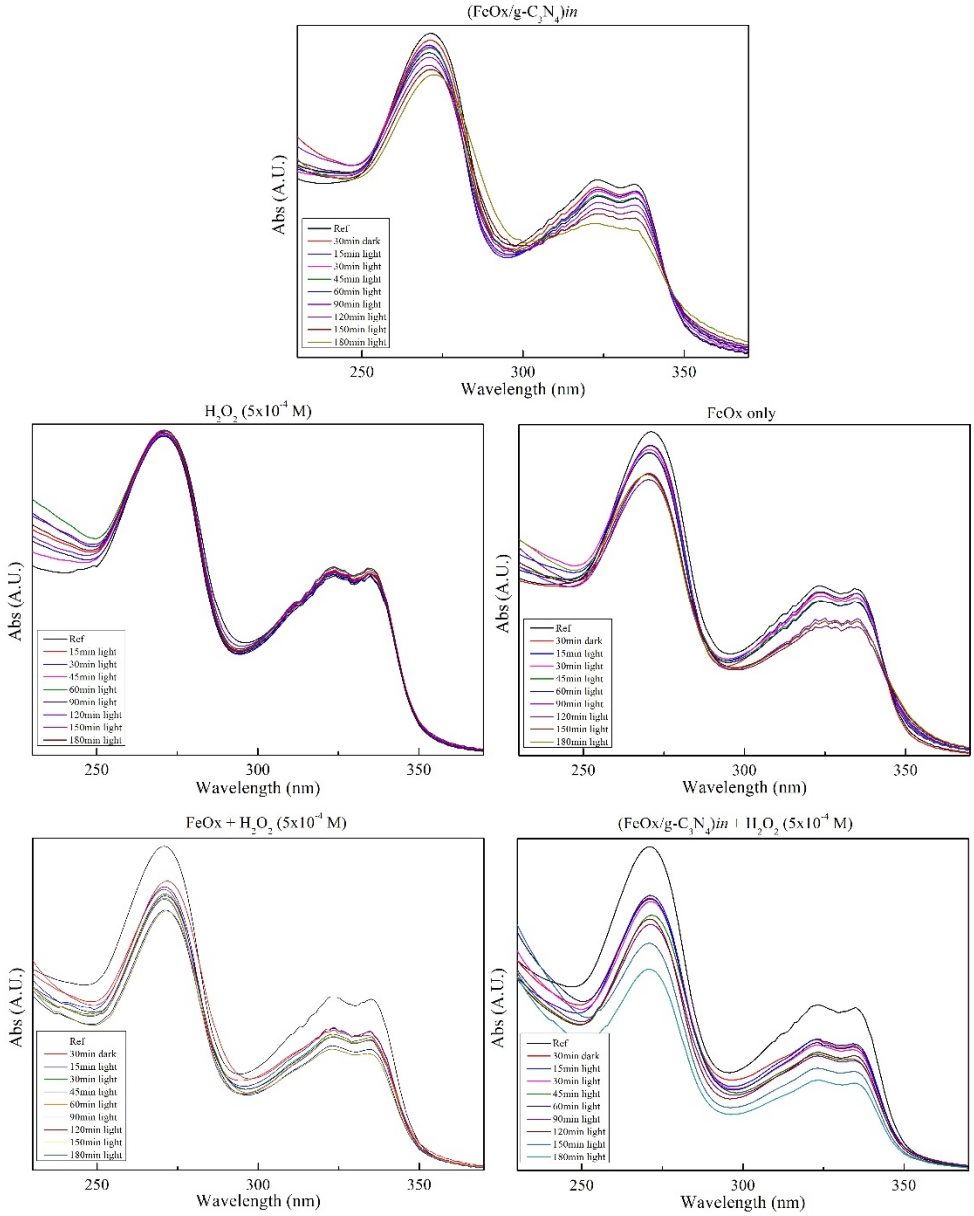

Figure S16. UV–visible spectra from obtained from the photocatalysis and photo-Fenton experiments.

References

[1] Y. Huang, B. Chen, J. Duan, F. Yang, T. Wang, Z. Wang, W. Yang, C. Hu, W. Luo, Y. Huang, Graphitic Carbon Nitride (g-C3N4): An Interface Enabler for Solid-State Lithium Metal Batteries, Angew. Chemie Int. Ed. 59 (2020) 3699–3704. https://doi.org/https://doi.org/10.1002/anie.201914417.

[2] X. Liu, W. Yang, L. Chen, Z. Liu, L. Long, S. Wang, C. Liu, S. Dong, J. Jia, Graphitic Carbon Nitride (g-C3N4)-Derived Bamboo-Like Carbon Nanotubes/Co Nanoparticles Hybrids for Highly Efficient Electrocatalytic Oxygen Reduction, ACS Appl. Mater. Interfaces. 12 (2020) 4463–4472. https://doi.org/10.1021/acsami.9b18454.

[3] W.-J. Ong, L.-L. Tan, Y.H. Ng, S.-T. Yong, S.-P. Chai, Graphitic Carbon Nitride (g-C3N4)-Based Photocatalysts for Artificial Photosynthesis and Environmental Remediation: Are We a Step Closer To Achieving Sustainability?, Chem. Rev. 116 (2016) 7159–7329. https://doi.org/10.1021/acs.chemrev.6b00075.

[4] Y. Wang, X. Zhang, X. Ding, Y. Li, B. Wu, P. Zhang, X. Zeng, Q. Zhang, Y. Du, Y. Gong, K. Zheng, X. Tian, Stitching Graphene Sheets with Graphitic Carbon Nitride: Constructing a Highly Thermally Conductive rGO/g-C3N4 Film with Excellent Heating Capability, ACS Appl. Mater. Interfaces. 13 (2021) 6699–6709. https://doi.org/10.1021/acsami.0c22057.

[5] L. Svoboda, P. Praus, M.J. Lima, M.J. Sampaio, D. Matýsek, M. Ritz, R. Dvorský, J.L. Faria, C.G. Silva, Graphitic carbon nitride nanosheets as highly efficient photocatalysts for phenol degradation under high-power visible LED irradiation, Mater. Res. Bull. 100 (2018) 322–332. https://doi.org/10.1016/j.materresbull.2017.12.049.

[6] Y. Zhang, Q. Pan, G. Chai, M. Liang, G. Dong, Q. Zhang, J. Qiu, Synthesis and luminescence mechanism of multicolor-emitting g-C3N4 nanopowders by low temperature thermal condensation of melamine, Sci. Rep. 3 (2013) 1–8. https://doi.org/10.1038/srep01943.

[7] J. Jiang, J. Zou, A.T.S. Wee, W. Zhang, Use of single-layer g-C3N4 /Ag hybrids for surface-enhanced raman scattering (SERS), Sci. Rep. 6 (2016) 1–10. https://doi.org/10.1038/srep34599.

[8] C.P. Marshall, W.J.B. Dufresne, C.J. Rufledt, Polarized Raman spectra of hematite and assignment of external modes, J. Raman Spectrosc. 51 (2020) 1522–1529. https://doi.org/https://doi.org/10.1002/jrs.5824.

[9] S. Tonda, S. Kumar, S. Kandula, V. Shanker, Fe-doped and -mediated graphitic carbon nitride nanosheets for enhanced photocatalytic performance under natural sunlight, J. Mater. Chem. A. 2 (2014) 6772–6780. https://doi.org/10.1039/C3TA15358D.

[10] R.J. Meier, J.R. Maple, M.-J. Hwang, A.T. Hagler, Molecular Modeling Urea- and Melamine-Formaldehyde Resins. 1. A Force Field for Urea and Melamine, J. Phys. Chem. 99 (1995) 5445–5456. https://doi.org/10.1021/j100015a030.

[11] M. Jelínek, J. Zemek, M. Trchová, V. Vorlíček, J. Lančok, R. Tomov, M. Šimečková, CNx films created by combined laser deposition and r.f. discharge: XPS, FTIR and Raman analysis, Thin Solid Films. 366 (2000) 69–76. https://doi.org/https://doi.org/10.1016/S0040-6090(00)00853-1.